

## Using CFD modelling to study hydraulic flow over labyrinth weirs

Anees K. Idrees <sup>a,\*</sup>, Riyadh Al-Ameri<sup>b</sup> and Subrat Das<sup>b</sup>

<sup>a</sup> Department of Environment Engineering, Faculty of Engineering, University of Babylon, Hillah-Najf Road, Babylon, Iraq

<sup>b</sup> School of Engineering, Faculty of Science Engineering & Built Environment, Deakin University, 75 Pigdons Road, Waurm Ponds, VIC 3220, Australia

\*Corresponding author. E-mail: aneeskadhum@gmail.com

 AKI, 0000-0002-8766-7953

### ABSTRACT

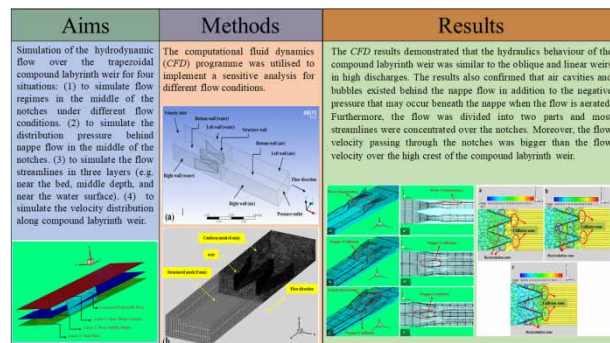
The compound labyrinth weir is a new type of labyrinth weir that is considered a good applicable choice for increasing the capacity of discharge. The flow over a compound labyrinth weir is a complex problem because the flow behavior is three-dimensional. The present study aims to simulate the flow over the compound labyrinth weir into the critical regions that cannot be observed when using an experimental test. The computational fluid dynamics (CFD) programme was utilised to implement a sensitive analysis for this purpose and under different flow conditions. The MAPE and RMSE indices were utilised to verify the CFD results with experimental work. The statistical indices of the maximum error ME, RMSE and MAPE were 4.7%, 0.033 and 3.9 respectively. Therefore, the findings showed that there is a good matching between the experimental and CFD results. The CFD results demonstrated that the hydraulics behaviour of the compound labyrinth weir was similar to the oblique and linear weirs in high discharges. The results also confirmed that air cavities and bubbles existed behind the nappe flow in addition to the negative pressure that may occur beneath the nappe when the flow is aerated. Furthermore, the flow was divided into two parts and most streamlines were concentrated over the notches. Moreover, the flow velocity passing through the notches was greater than the flow velocity over the high crest of the compound labyrinth weir.

**Key words:** aeration, compound labyrinth weir, computational fluid dynamics (CFD), pressure, streamline, velocity

### HIGHLIGHTS

- The flow regimes under different flow conditions at the middle of the compound labyrinth weir were simulated.
- The pressure distribution behind nappe flow at the middle of the compound labyrinth weir was simulated.
- The flow streamlines and water surface profile at three layers of the compound labyrinth weir were simulated
- The velocity distribution along the compound labyrinth weir was simulated.

### GRAPHICAL ABSTRACT



This is an Open Access article distributed under the terms of the Creative Commons Attribution Licence (CC BY 4.0), which permits copying, adaptation and redistribution, provided the original work is properly cited (<http://creativecommons.org/licenses/by/4.0/>).

## NOTATIONS

The symbols are utilised in this work as follows:

A	Inside apex width
b1	Bottom width of the notch
B	Labyrinth weir length in the flow direction
$C_{dc}$	Compound coefficient of discharge, data were from the current study
D	Outside apex width
g	Gravity acceleration
$L_c$	Total centerline length of labyrinth weir
lc	Centerline length of a side wall
Lc-cycle	Centerline length for a single labyrinth weir cycle
l'	Length of the notch
$L'_c$	Labyrinth weir crest length after subtracting the length of notches ( $\Delta L$ ), ( $L'_c = L_c - n * \Delta L$ )
MAPE	Mean Absolute Percentage Error
N	Number of labyrinth weir cycles
n	Number of notches
P	Weir height
P'	Notch height
Q	Discharge over the weir
RMSE	Root Mean Square Error
$t_w$	Wall thickness of the labyrinth weir
$y_c$	Critical depth over compound labyrinth weir
V	Mean flow velocity at upstream of the labyrinth weir
W	Channel width
w	Single labyrinth weir cycle width
$\Delta L$	The top width for the notch
$\Delta P$	The notch depth
$V_0$	Upstream mean velocity
$\alpha$	Sidewall angle

## INTRODUCTION

Labyrinth weirs are a good choice to increase the capacity of flow per unit of the weir width for a given water level. Recently, compound labyrinth weirs are being used more efficiently than conventional labyrinth weirs for increasing discharge capacity (Idrees *et al.* 2016). It seems that the modified labyrinth weir can be a promising solution that can be applied successfully. However, many factors impact on the labyrinth weir capacity that cause the complex design of the overflow structure. The main impact factors are the weir shape in planform, crest shape, the weir height, sidewall angle, head over the crest, sidewall thickness, apex shape, and approach channel conditions (Crookston 2010).

The computation fluid dynamic (CFD) program is currently widely used in water resources applications and is utilised in combination with other methods such as physical modelling. Versteeg & Malalasekera (1995) showed that CFD can be a good option to solve and analyse a problem rather than producing a final result, mainly due to the number of suppositions used in the numerical methods to find results in CFD. The flow becomes more complicated in the modelling process when the flow is three-dimensional (3D) (Ghare *et al.* 2008).

Recently, studies have been interested in using CFD modelling as an additional design tool for labyrinth weirs (Shaghaghian & Sharifi 2015; Daneshfaraz *et al.* 2016, 2019; Seo *et al.* 2016; Hu *et al.* 2018; Sangsefidi *et al.* 2019). A limited number of numerical researches have been achieved to date on the hydraulic characteristics of labyrinth weirs. Savage *et al.* (2004) conducted a numerical study and compared it to studies of physical models carried out by the US Bureau of Reclamation (USBR). They found that existing design methods were incomplete for labyrinth weirs with varying  $P$  values. Bhuiyan & Hey (2007) carried out a numerical study to simulate experimental tests in a straight channel for three shapes of weirs. The study aimed to investigate flow directions with respect to folder weirs. Simulated and measured velocity profiles were compared at different locations downstream of a linear rectangular weir. Paxson *et al.* (2008) investigated the possibility of a replacement gate for the spillway for Lake Townsend Dam by another labyrinth weir based on weir efficiency in passing a large storm event. Experiments were conducted on numerical and physical models of the labyrinth weir. The finite-volume method, which is available in Flow-3D in CFD, was applied as a numerical technique. Lopes *et al.* (2008) provided guidance for calculating energy

dissipation downstream of a labyrinth weir. Ackers *et al.* (2011) used the empirical equation of Tullis *et al.* (1995) for the hydraulic design of the labyrinth weir and studied the flow behaviour using ANSYS CFX-12 software as a tool of the CFD. Holmquist-Johnson (2011) utilised a three-dimensional numerical model to investigate the effect of alternative solutions in U-weir geometry on local hydraulics (downstream bed shear stress, velocity and upstream water surface elevations). Sangsefidi *et al.* (2015) conducted a numerical study using Flow-3D software as a tool of the CFD to study the impact of the downstream bed level on the coefficient of discharge of linear and arced labyrinth spillways. The results demonstrated that in the case of a high headwater, the coefficient of discharge increased when the downstream bed level of the labyrinth spillway reduced, especially in the case of an arced labyrinth spillway. Savage *et al.* (2016) used numerical and physical modelling to investigate the flow characteristics with high headwater in labyrinth weirs. The results showed that CFD modelling was able to precisely simulate flow characteristics in labyrinth weirs and calculated discharges were fairly independent of the turbulence model. Torres *et al.* (2018) used the CFD package to validate results in physical models and compared between two solvers. Salazar & Crookston (2019) estimated the discharge for arced labyrinth spillways using experimental data and machine learning algorithms. Bilhan *et al.* (2018) carried out an experimental and numerical study by using CFD modelling to study the impact of nappe breakers on the capacity of discharge and subatmospheric pressure under the nappe flow. The results of both the experimental observations and numerical simulations demonstrated the positive results found through the utilise of the nappe breakers to control subatmospheric pressures on the downstream face of the circular labyrinth weirs. Carrillo *et al.* (2019) carried out numerical simulations by CFD modelling and experimental work for a large sidewall angle of a labyrinth weir under free flow and submerged flow, utilising three different turbulence models.

Carrillo *et al.* (2020) conducted a numerical study to show the effect of submerged and free flows on the coefficient of discharge over labyrinth weirs. They also analysed the free surface flow profile in the downstream and upstream reaches of the labyrinth weir. The outcomes demonstrated that CFD models can provide fairly well predictions of the coefficient of discharge on submerged and free flow over labyrinth weirs for a large sidewall angle. Shafiei *et al.* (2020) carried out the study to simulate the coefficient of discharge of labyrinth weirs utilising the CFD model, adaptive neuro-fuzzy inference system (ANFIS) and a hybrid approach of the ANFIS-FFA. The outcomes confirmed that the ANFIS-FFA model was significantly more accurate in estimating the coefficient of discharge. Pourshahbaz *et al.* (2020) used FLOW-3D software as a tool of the CFD. They investigated numerical modelling and hydro-morphological of a group of parallel groynes which were stationed vertically. The authors found that the critical velocity ratio ( $U_{avg}/U_{cr}$ ) and the approach Froude number was an impact on the accuracy of the simulation of the FLOW-3D model. Ghaderi *et al.* (2020) adopted RNG  $k-\epsilon$  model and the volume of fluid (VOF) method in the FLOW-3D software to simulate the free flow surface over the labyrinth weir. They confirmed that the numerical model was good to predict the flow over the labyrinth weir and a maximum relative error was 4.8%. They found that the hydraulic performance of the modified labyrinth weir was better when compared to a conventional labyrinth weir. Yildiz *et al.* (2021) carried out experimental work and numerical model by ANSYS-Fluent program as a tool of the CFD for different heights and shapes of labyrinth weirs. They found that the discharge coefficient ( $C_d$ ) decreases when the number of triangles ( $N$ ) of the weir increases. The outcomes also demonstrated that the height of the weir ( $P$ ) does not have a significant impact on the capacity of discharge.

Nevertheless, numerical tools still have limitations such as run times, aeration, representation of turbulence, numerical instabilities, and grid resolution. But numerical modelling in some of the regions of the weir may be more precise than a physical model. Also, numerical models can give more understanding about distributions of pressure and velocity than a physical model. In addition, numerical models may be more economical in some cases. Therefore, the present study aims to simulate hydrodynamic flow over the trapezoidal compound labyrinth weir for four situations: (1) to simulate flow regimes in the middle of the notches under different flow conditions; (2) to simulate the distribution pressure behind nappe flow in the middle of the notches; (3) to simulate the flow streamlines in three layers (e.g. near the bed, middle depth, and near the water surface); (4) to simulate the velocity distribution along a compound labyrinth weir. To the knowledge of the authors, the present study has been used CFD approaches to introduce new information about a sensitive analysis of the hydrodynamic flow over compound labyrinth weir for different layers of the flow which cannot be observed by experiment tests with different flow conditions.

## MATERIALS AND METHODS

### Experimental method

Current experimental work was achieved in the hydraulic laboratory at Deakin University in Australia. The experimental work involves a rectangular flume of width 0.5 m length 7 m and height 0.6 m. The discharges were supplied to the flume

through a 200 mm diameter pipe and using two pumps connected in parallel. The capacity of each pump was 40 L/s, giving a total capacity of 80 L/s for both. A flow meter was utilised to measure the rate of the discharges. The discharges were measured by a flow meter that was installed in the main pipeline. The bed slope of the flume was set to horizontal. The flume also contains one regulating gate downstream to control the tailwater elevation. Wave suppressors were provided upstream of the flume. Wave suppressors were used for controlling the flow and dissipating the surface disturbances. The flow rates for each test were controlled by a gate valve. All tests used a fully open gate. A schematic of the rectangular flume test facility is given in Figure 1. The geometry of the model consisted of two cycles ( $N=2$ ) and Table 1 shows the model geometry for the experimental and CFD model. The physical model was fabricated with an acrylic sheet of 10 mm thickness ( $t_w$ ). The acrylic sheets were cut using a laser machine to obtain precise dimensions and then the parts were assembled using screws. Silicon was used to prevent the leakage of water through all joints of the models.

To certify that the model is valid, five values of flow rates were used for a physical model. These values varied from low to high discharge (e.g.  $Q = 0.005, 0.02, 0.04, 0.06, 0.1 \text{ m}^3/\text{s}$ ). A movable pointer gauge with an accuracy of  $\pm 0.001 \text{ m}$  was located to flume on distance  $5P$  (approximately 100 cm) of the downstream of the physical models to measure the downstream water level ( $h_1$ ). This position has been used to reduce the effect of turbulent characteristics of the flow and the visual position; thus, flow is more stable to yield high accuracy during testing as recommended by Dabbling (2014). The upstream water depth in the flume was determined to utilise the point gauge device, and the bed of the flume was used as a reference. For each run conducted on a physical model, the pump was started at a given flow rate by handling the flow control valve. The flume was filled with water and waited 30 minutes before starting the test to stabilise flow and to maintain thermal contraction/expansion. This method allows for water depths and discharges to be measured accurately.

Measurements were collected by adjusting the discharge rate ( $Q$ ) and measuring the water level ( $h_1$ ) downstream of the weir. To guarantee the flow is in steady-state conditions, measurements were not taken until a satisfactory amount of time had passed, which was at least 4 min as recommended by Crookston (2010). The velocity of flow was calculated by dividing the actual discharge value, which was measured via a flow meter, to the cross-section area of flow. That was based on the width of the channel and water level ( $h_1$ ) at downstream of the labyrinth weir. The outlet velocity of the weir ( $V_1$ ) has been obtained from the physical model test and has been compared with the same outlet velocity value as the CFD model. Figure 2 also presents the details of the 3D trapezoidal compound labyrinth weir and plan view of common geometry.

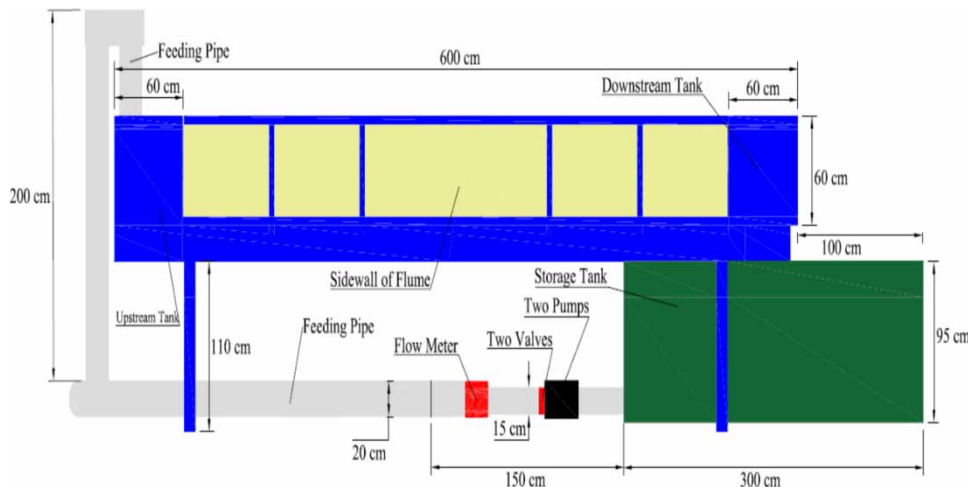


Figure 1 | Schematic of the rectangular flume test facility, all dimension in centimetres.

Table 1 | Model geometry for the experimental and CFD model

$\alpha(^{\circ})$	$P \text{ cm}$	$P' \text{ cm}$	$B \text{ cm}$	$Lc \text{ cm}$	$A \text{ cm}$	$D \text{ cm}$	Notch geometry				Crest Shape	
							$b1 \text{ cm}$	$\Delta L \text{ cm}$	$\Delta P \text{ cm}$	$\Delta P/P$		$\Delta L/Lc$
10	20	16	60.4	253.5	2	3.6	28.8	36.8	4	0.2	0.6	FC



where  $A_x$ ,  $A_y$ , and  $A_z$  are fractional areas open to flow in the  $x$ -,  $y$ -, and  $z$ -direction respectively; and  $u$ ,  $v$ , and  $w$  are velocity components in the  $x$ -,  $y$ -, and  $z$ -direction respectively.

The Navier-Stokes equations with velocity components as the momentum equations are utilised to define three-dimensional fluid mobility for Cartesian coordinates (Bilhan *et al.* 2018):

$$\left. \begin{aligned} \frac{\partial u}{\partial t} + \frac{1}{V_F} \left[ uA_x \frac{\partial u}{\partial x} + vA_y \frac{\partial u}{\partial y} + wA_z \frac{\partial u}{\partial z} \right] &= -\frac{1}{\rho} \frac{\partial p}{\partial x} + G_x + f_x \\ \frac{\partial v}{\partial t} + \frac{1}{V_F} \left[ uA_x \frac{\partial v}{\partial x} + vA_y \frac{\partial v}{\partial y} + wA_z \frac{\partial v}{\partial z} \right] &= -\frac{1}{\rho} \frac{\partial p}{\partial y} + G_y + f_y \\ \frac{\partial w}{\partial t} + \frac{1}{V_F} \left[ uA_x \frac{\partial w}{\partial x} + vA_y \frac{\partial w}{\partial y} + wA_z \frac{\partial w}{\partial z} \right] &= -\frac{1}{\rho} \frac{\partial p}{\partial z} + G_z + f_z \end{aligned} \right\} \quad (2)$$

where  $V_F$  is volume fraction open to flow;  $G_x$ ,  $G_y$ , and  $G_z$  are components of body acceleration; and  $f_x$ ,  $f_y$ , and  $f_z$  are components of viscous accelerations. For defines fluid configurations, the volume of fluid (VOF) function represents a fluid volume of 1 per unit volume as given in Equation (3) (Hirt & Nichols 1981):

$$\frac{\partial F}{\partial t} + \frac{\partial 1}{V_F} \left[ \frac{\partial}{\partial x} (FA_x u) + R \frac{\partial}{\partial y} (FA_y v) + \frac{\partial}{\partial z} (FA_z w) + \varphi \frac{FA_x u}{x} \right] = F_D + F_S \quad (3)$$

where  $F_D$  is the diffusion term, included only for the turbulent mixing in a two-phase flow application; and  $F_S$  is a source of the density. These two distinctive incompressible flow models were utilised to describe the flow characteristics of the trapezoidal compound labyrinth weir. The two-phase model (air and water) was applied for discharge performance and pressure characterization, specifically the sub-atmospheric pressures behind the nappe. The standard  $k-\epsilon$  model solves two transport equations with Reynolds stresses for the turbulence kinetic energy ( $k$ ) and dissipation rate ( $\epsilon$ ). The standard  $k-\epsilon$  model is most commonly utilised in CFD applications (Bilhan *et al.* 2018). The standard  $k-\epsilon$  model is dependent on the suppositions that viscous impacts are negligible, and the flow is fully turbulent. The standard  $k-\epsilon$  model is described in the following (Kheirkhah 2013; Shaheed *et al.* 2019).

$$\frac{\partial k}{\partial t} + \frac{\partial k u_i}{\partial x_i} = \frac{\partial}{\partial x_i} \left( Dk_{eff} \frac{\partial k}{\partial x_i} \right) + G_k - \epsilon \quad (4)$$

$$\frac{\partial \epsilon}{\partial t} + \frac{\partial \epsilon u_i}{\partial x_i} = \frac{\partial}{\partial x_i} \left( D\epsilon_{eff} \frac{\partial \epsilon}{\partial x_i} \right) + C_{1\epsilon} \frac{\epsilon}{k} G_k - C_{2\epsilon} \frac{\epsilon^2}{k} \quad (5)$$

where  $G_k$  is the generation of turbulent kinetic energy due to mean velocity gradients, and  $Dk_{eff}$  and  $D\epsilon_{eff}$  are the effective diffusivity for turbulence kinetic energy ( $k$ ) and dissipation rate ( $\epsilon$ ), respectively, which are computed as the following:

$$Dk_{eff} = \nu + \nu_t \quad (6)$$

$$D\epsilon_{eff} = \nu + \frac{\nu_t}{\sigma_\epsilon} \quad (7)$$

For calculating the turbulent kinematic viscosity at each point is shown by Equation (8):

$$\nu_t = C_\mu \frac{k^2}{\epsilon} \quad (8)$$

where  $\sigma_\epsilon$  is the turbulent Prandtl number for  $\epsilon$  and is given as a value equal to 1.3. Moreover, the constants  $C_{1\epsilon}$ ,  $C_{2\epsilon}$  and  $C_\mu$  have the following values:

$$C_{1\epsilon} = 1.44, C_{2\epsilon} = 1.92, C_\mu = 0.09$$

$G_k$  is the found of turbulent kinetic energy, which is common in most turbulence models, and is given by Equation (9):

$$G_k = 2\nu_t S_{ij}^2 \quad (9)$$

where the strain-rate tensor  $S_{ij}$  is given by Equation (10):

$$S_{ij} = 0.5 \left( \frac{\partial u_j}{\partial x_i} + \frac{\partial u_i}{\partial x_j} \right) \quad (10)$$

### Geometry, mesh, and boundary conditions

For simulating the experimental work in FLUENT correctly, the model geometry was formed in three dimensions, and the analysis was carried out in three dimensions. Therefore, the model geometry was used in the *CFD* program the same as the physical model. The conservation of mass, energy, and momentum must be applied over the zone (Institute for Water and Environmental Engineering 2012).

The mesh grid can be created of either quadrilateral, tetrahedrons or a combination of both, and a cut cell mesh is used for this scenario. In the present study, the mesh grid was created of quadrilaterals with two different mesh blocks. Hence, a combination mesh block was created according to the interest area such as the region of the flow over the labyrinth weir (see Figure 3(b)). This technique was adopted by Choufu *et al.* (2019). The shape of the mesh utilised in the analysis has highly significant importance. The shape of flow volume is the effect on the total number of elements, the analysis time and the analysis accuracy.

The simulation of models using a tetrahedron mesh could not complete the solution successfully because the solution diverged continually. In contrast, the cut cell mesh process was stable because it required fewer elements. Therefore, using the combination mesh was a good option and was successful. However, a combination mesh generated a significant number of nodes and led to an increasing simulation run time. In the current study, different approaches were considered to find an appropriate mesh. Table 2 showed the mesh sensitivity analysis by comparison of the downstream velocity found from experimental results with numerical solutions. Five various mesh sizes have been applied for the labyrinth weir geometry and flume body. The optimal meshes and the suitable number were chosen (see Figure 4). According to

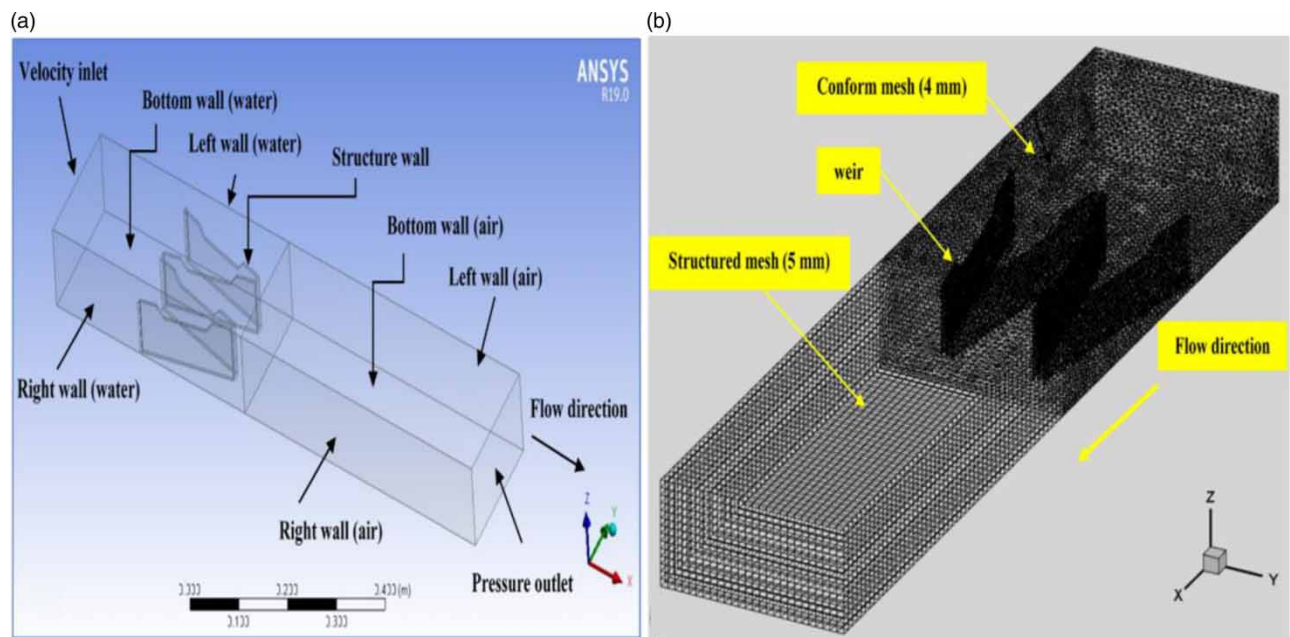


**Figure 3** | CFD modeling: (a) Geometry constructed for mathematical modelling, (b) view of the created mesh, illustrating a conforming mesh and structured mesh,  $\alpha = 10^\circ$ .

**Table 2** | Mesh sensitivity analysis for the current study

Test No.	Turbulence model	Cells size (cm)	Total mesh number	MAPE (%) = $100 \times \frac{1}{n} \sum_1^n \left  \frac{X_{exp} - X_{num}}{X_{exp}} \right $	RMSE = $\sqrt{\frac{1}{n} \sum_1^n (X_{exp} - X_{num})^2}$
1	<i>k</i> - $\epsilon$ (standard)	0.80	950,386	18.33	0.074
2	<i>k</i> - $\epsilon$ (standard)	0.7	1,155,600	10.23	0.056
3	<i>k</i> - $\epsilon$ (standard)	0.6	1,500,396	6.54	0.034
4	<i>k</i> - $\epsilon$ (standard)	0.5	1,790,500	2.78	0.023
5	<i>k</i> - $\epsilon$ (standard)	0.4	2,730,114	2.15	0.020

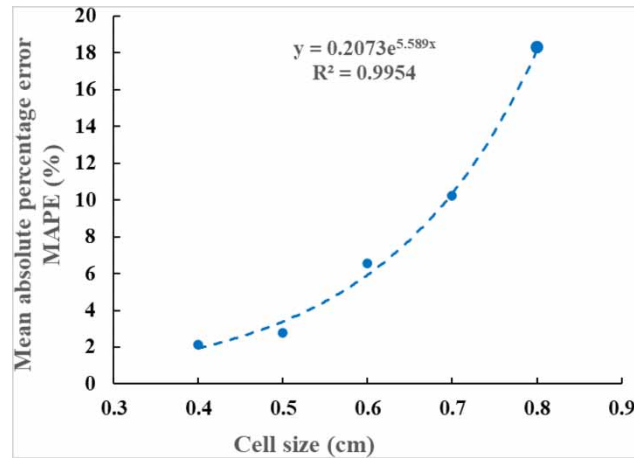
**Figure 4** | The variations of the Mean absolute percentage error % (MAPE) for outlet velocity of the labyrinth weir against cell size.

Figure 4, which presents the difference of the mean absolute percentage error % (MAPE) as a function of the cell sizes for the downstream velocity of the labyrinth weir, we can notice that the simulated downstream velocity showed a better agreement with the measured downstream velocity for the cell size of 0.4 cm. In addition, the variation of the mean absolute percentage error % (MAPE) can be neglected by reducing the cell size from 0.50 to 0.40 cm. In summary, to reduce the number of cells in the meshing process as far as possible, two types of mesh were selected depending on the importance of the areas. A mesh size of 0.4 cm is chosen and the total number of elements were 2,730,114 (0.4 cm in all directions). A mesh size of 0.4 cm has been selected in important zones such as water surface zones, intricate regions, in addition to regions where the values computed by the nodes were considered integral to the results. Whereas the cell size of 0.5 cm is chosen and the total number of elements was 1,790,500 (0.5 cm in all directions). A mesh size of 0.5 cm has been selected in the least important areas, as shown in Figure 3(b).

The boundary conditions have been described the same as the experimental conditions. The inlet boundary condition was set as the inlet velocity and the outlet boundary condition was set as the pressure outlet. Wall roughness has been neglected due to the small roughness of the material of the experimental facility which was used for validation. The channel walls were treated as shown in Figure 3(a). An atmospheric boundary condition was set to the upper boundary of the channel, which was set to zero. This allows the flow to enter and leave the domain.

### Model setup

In the present study, the model geometry is drawn by the Auto CAD program and exported to FLUENT. The mesh is created in the meshing programme. As mentioned, the meshing process is imported into the solver programme, and there is a number of settings that need to be set up with the details of the whole model. The volume of the fluid model was chosen. Also, the implicit scheme was selected, and implicit body forces were enabled. Within the setup of the models, all other values were left as default values. A *k*- $\epsilon$  (standard) model was selected for turbulence modelling, and the number of Eulerian phases was set to two. The air was set as the primary phase, and water was set as the secondary phase. According to the two phases of air and water, the values of density and viscosity were set as defaults, and they have adopted a reference

temperature of 25° because it was adequately close to the water temperature that was taken during the tests of the physical modelling (22°).

### Tests conducted

Flat crest and sidewall angles ( $\alpha$ ) of 10° were used for *CFD* simulation. Five values of flow rates were used for running. Each run has been taking a long time to complete the results. Therefore, further trials were achieved to find mesh suitability to use during the simulations process to reduce operation time.

For the tests run, the transient state was established, and an implicit model is selected for a large number of iterations with a regular flow rate. The solution convergence was depended on the uniformity and closeness to zero of the bulk equilibriums between the inflow and the outflow of the model. As the bulk equilibrium approaches zero, an acceptable tolerance is within 1% of the inlet flow. The data were recorded for 2000 iterations at the end report, and this was conducted to check the solution convergence. The outlet boundary condition was set to the pressure outlet of a flume setting, and the water depth in the outlet of the flume was set to help the simulations be stable. The transient model was run versus time in addition to time step was set. A small-time step was required to achieve the simulation process with more accuracy. However, in the present simulation, a time step size of 0.001s was used. The *CFD* program has been taken a long time to complete the solutions although it used a fast computer. Specification of the computer was included 128 gigabytes of random-memory (*RAM*) with quad-core dual processors, with a processing speed of 2.9 gigahertz and 10 terabits of external storage.

## RESULTS AND DISCUSSIONS

### Verification of the *CFD* model

According to the results obtained by *CFD*, the experimental approach defines velocity downstream of compound labyrinth weirs. The numerical solvers for compound labyrinth weir were at the starting of their developments. Therefore, there is a strong requirement validating the results. Also, the flow interpretation was still necessary for solver improvements. However, in the present study, there was a numerical study as a parallel work to experimental study. The root means square error (*RMSE*), (Equation (11)), and the mean absolute percentage error (*MAPE*) (Equation (12)) are the criteria that have been utilised to validate the numerical models.

$$RMSE = \sqrt{\frac{1}{n} \sum_{i=1}^n (X_{experimental} - X_{numerical})^2} \quad (11)$$

$$MAPE = 100 \times \frac{1}{n} \sum_{i=1}^n \left| \frac{X_{experimental} - X_{numerical}}{X_{experimental}} \right| \quad (12)$$

A coefficient of correlation is a tool that is utilised to determine the goodness of fit and the relative correlation between the observed and numerical results. It can be computed as given by Equation (13):

$$R = \frac{C_{yjdj}}{\sigma_{yj} \sigma_{dj}} \quad (13)$$

$$C_{yjdj} = \frac{1}{n-1} \sum_{j=1}^n (y_j - \bar{y})(d_j - \bar{d}) = \frac{1}{n-1} \left\{ \sum_{j=1}^n y_j d_j - \frac{\sum_{j=1}^n y_j \sum_{j=1}^n d_j}{n} \right\} \quad (14)$$

$$\sigma_{yj} = \sqrt{\frac{\sum_{j=1}^n (y_j - \bar{y})^2}{n-1}} \quad (15)$$

$$\sigma_{dj} = \sqrt{\frac{\sum_{j=1}^n (d_j - \bar{d})^2}{n-1}} \quad (16)$$

Here,  $y_i$  and  $d_j$  are defined as the numerical and experimental output results, respectively;  $C_{yjdj}$  is the covariance between the *CFD* ( $y_j$ ) and the physical model results ( $d_j$ );  $\sigma_{yj}$  and  $\sigma_{dj}$  are the standard deviations of the *CFD* and the physical model

results, respectively;  $\bar{y}$  and  $\bar{d}$  are the means of the *CFD* and the physical model results, respectively, and  $n$  is the number of results. Smith (1986) recommended the following guide for the value of ( $R$ ) between 0.0 and 1.0.

- $|R| \leq 0.2$  means there is a weak correlation between two sets of variables.
- $0.2 < |R| < 0.8$  means there is a correlation between two sets of variables.
- $|R| \geq 0.8$  means there is a strong correlation between two sets of variables.

The *CFD* model was set with boundaries of the pressure, and the *CFD* solver verified the matching of the velocities values downstream of the physical model. The velocity values downstream of the weir ( $V_1$ ) have been obtained from *CFD* analyses and physical model results as shown in Figure 5. Figure 5 exhibits the relationship between the velocity downstream of the weir and the critical depth ( $y_c$ ) of total flow passing over the weir that is calculated by Equation (17).

$$y_c = \sqrt[3]{\frac{q^2}{g}} \quad (17)$$

where  $y_c$  is the critical depth of total flow passing over the labyrinth weir,  $q$  is flow per unit meter, and  $g$  is gravity acceleration. Figure 5 demonstrated that there is a good matching between the experimental and *CFD* modelling results and the maximum error was 4.7%. This proved the ability of the *CFD* model to predict the flow characteristics over the compound labyrinth weir. Also, for the experimental/numerical comparison, statistical measures such as the correlation coefficient ( $R$ ), *MAPE*, and *RMSE* were computed as shown in Table 3.

The benefit of utilising *MAPE* and *RMSE* indicators that calculate scale results of these errors are the unit scale of the experimental parameter, and their ideal values are both zero. In other words, the model that has a value of this index nearest to zero should be considered more precise. As shown in Table 3, the *MAPE* and *RMSE* indices demonstrated the difference between the experimental and *CFD* data. The results demonstrated that the *MAPE* index is 3.9 for five different discharge rates, and the *RMSE* index is closer to zero, signifying better agreement.

## Flow regime

The results of the *CFD* modelling include a numerical technique to simulate flow regimes under different flow conditions. Figure 6 shows the slice location in the middle of the compound labyrinth weir. A slice location was at a distance of 30 cm from the upstream apex of the compound labyrinth weir. The purpose of selecting the slice location in the middle of the notch was to provide a clearer understanding of the nappe-flow conditions such as aerated, partially aerated, and drowned over a compound labyrinth weir. This information obtained from the analysis of the results highlights the critical areas that cannot be observed by experimental tests, and this information should be considered when designing the compound labyrinth weir structure.

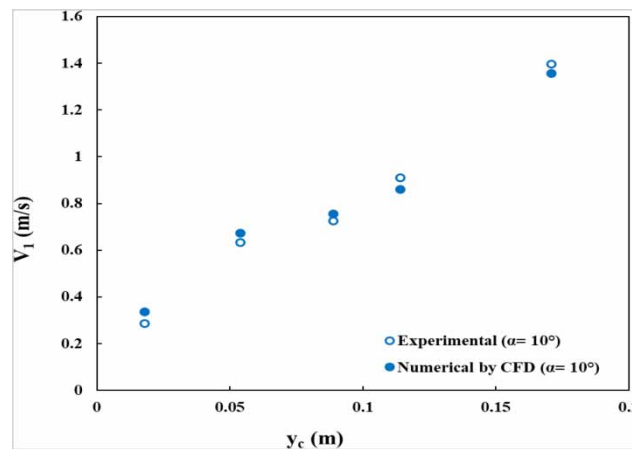


**Figure 5** | Experimental and numerical velocity at downstream ( $V_1$ ) against critical depth ( $y_c$ ) for flat top crest of compound labyrinth weir and  $\alpha = 10^\circ$ .

**Table 3** | The statistical measures of numerical and experimental results for sidewall angle ( $\alpha = 10^\circ$ ) of compound labyrinth weir and five different discharge rates

$\alpha$	$Q^a$ m <sup>3</sup> /s	Experimental results $V_1^b$ m/s	CFD modelling results $V_1^c$ m/s	The relative error %	RMSE <sup>d</sup>	MAPE <sup>e</sup> %	Correlation ( <i>R</i> )
10°	0.004	0.33	0.34	3.0	0.033	3.9	0.991
	0.02	0.634	0.66	4.1			
	0.04	0.724	0.758	4.6			
	0.06	0.911	0.868	4.7			
	0.11	1.397	1.356	2.9			
			Mean	3.8			

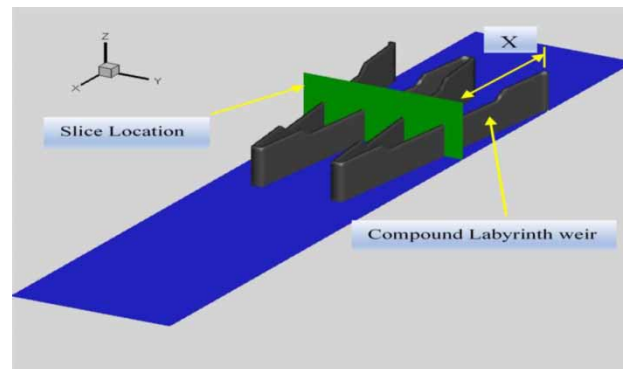
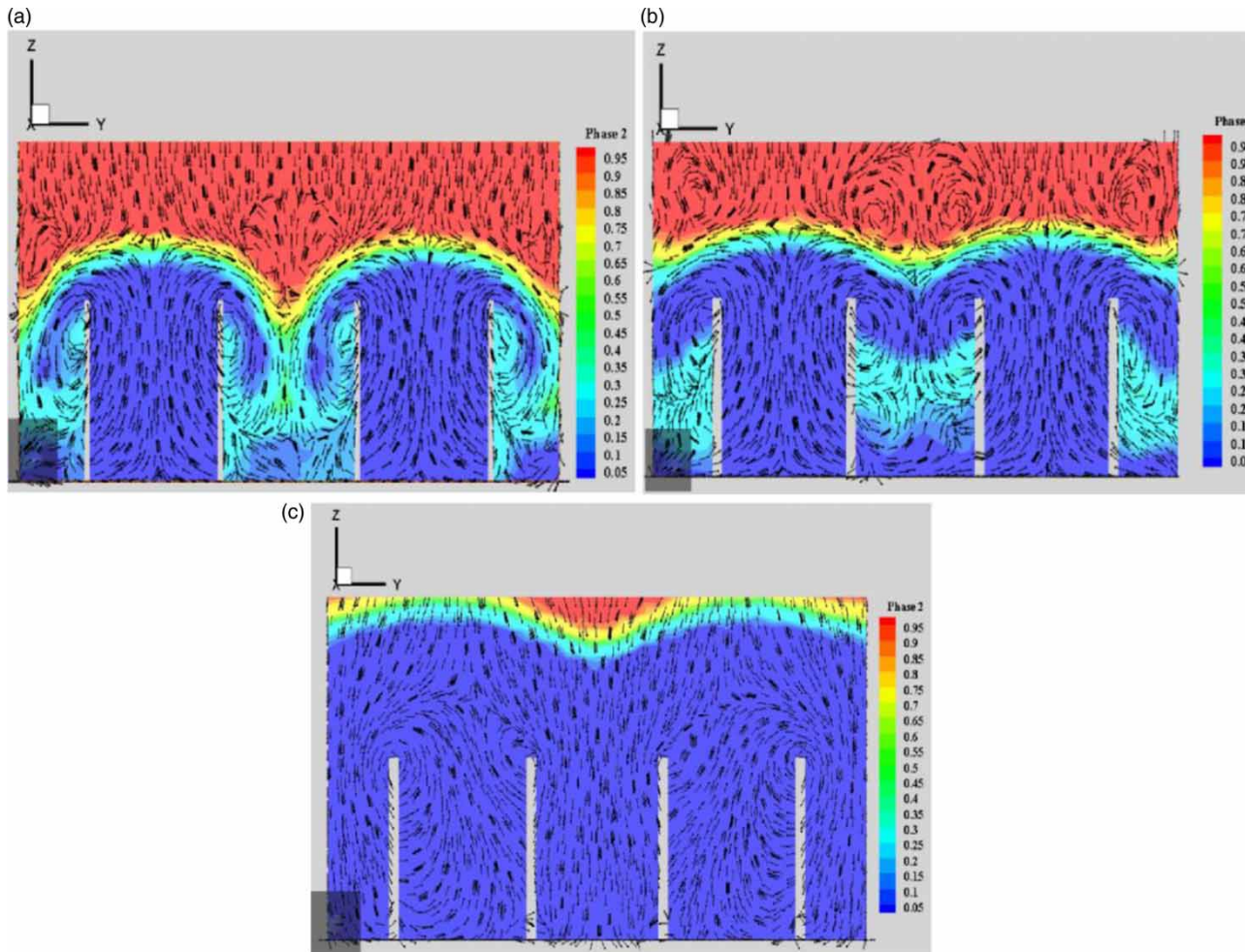
<sup>a</sup> $Q$ , discharge m<sup>3</sup>/s.<sup>b</sup> $V_1$ , velocity at downstream from experimental results m/s.<sup>c</sup> $V_1$ , velocity at downstream from CFD results.<sup>d</sup>RMSE, Root Mean Square Error.<sup>e</sup>MAPE, Mean Absolute Percentage Error.**Figure 6** | Location of the slice in the middle of the compound labyrinth weir.

Figure 7 presents aeration gradients and vortices vectors for the nappe-flow conditions when it is aerated, partially aerated, and drowned for  $\alpha = 10^\circ$ . Three different discharges were selected to representing nappe-flow conditions (e.g.  $Q = 0.02$  m<sup>3</sup>/s,  $0.04$  m<sup>3</sup>/s and  $0.06$  m<sup>3</sup>/s). In case of discharge ( $Q$ ) =  $0.02$  m<sup>3</sup>/s, the nappe-flow condition was aerated, as occurred in the experiments works. This case was reproduced by the numerical model, as illustrated in Figure 7(a). The modelling results showed that the air cavities and the bubbles exist, as is described by the cyan colour. The results demonstrated that the numerical model results correspond to observations of the physical model. In contrast, in the case of discharge ( $Q$ ) =  $0.04$  m<sup>3</sup>/s, the nappe-flow condition was partially aerated, as occurred in the experiments works. This case was reproduced by the numerical model. From the modelling results, the air cavities and the bubbles exist, but they are separated and distributed in different regions behind nappe flow, as explained by the cyan colour and illustrated in Figure 7(b). Also, the outcomes showed that the numerical model results are similar to observations of the physical model. When nappe flow reaches a drowning stage, the air cavities and bubbles were absent, as illustrated in Figure 7(c). The results also showed that the numerical model results are similar to observations of the physical model. In addition, the nappe trajectory develops to be nearer to the weir faces. The simulation was performed at  $Q = 0.02$  m<sup>3</sup>/s. This discharge is used to drive the nappe to separate from the weir face of a physical model when the weir is in an aerated condition. In contrast, Figure 7 represented the vortices via velocity vectors in the middle of the notches. The vector size provides a relative measure of the velocity magnitude. Velocity vectors have demonstrated the clear occurrence of the vortices behind the nappe flow and base of the weir, as illustrated in Figure 7. The results demonstrated that part of the energy dissipation occurs in these regions because of local turbulent water. Also, these figures showed that the nappe-flow conditions change from aerated to nonaerated when increasing the discharge. The shape and size of vortices change with increased discharge.



**Figure 7** | Aeration gradients and velocity vectors for the nappe flow conditions (a) aerated, (b) partially aerated and (c) drowned. For  $\alpha = 10^\circ$  and  $Q = 0.02 \text{ m}^3/\text{s}$ ,  $0.04 \text{ m}^3/\text{s}$  and  $0.06 \text{ m}^3/\text{s}$ , respectively.

### Pressure simulation behind nappe flow

The pressure behind the nappe was simulated by using slices (cross-section) in the middle of a notch of the compound labyrinth weir. The cross-section was located 30 cm of the upstream apex, as shown in Figure 6. Figure 8 shows the pressure distribution behind the nappe under different flow conditions when it is aerated, partially aerated, and drowned. Three different discharges were selected for representing nappe-flow conditions (e.g.  $Q = 0.02 \text{ m}^3/\text{s}$ ,  $0.04 \text{ m}^3/\text{s}$  and  $0.06 \text{ m}^3/\text{s}$ ). Figure 8 also shows the pressure distributions via rainbow scale colouring and shows that pressure increases as discharge increases. The model indicated that the pressure distribution behind the nappe increases toward the base of the weir.

The simulation in the middle of the compound labyrinth weir is important because it reflects what is occurring in this region of changes in the pressures between upper and lower surfaces. Furthermore, it is important to determine the size and location of the low-pressure zones that directly influence the trajectory of the nappe and its effect on the hydraulic characteristics of the weir (Savage *et al.* 2016). In this context, negative pressure may occur beneath nappe flow when the flow is in an aerated condition because nappe thickness is small and air cavities behind nappe are connected or closer to the atmosphere, as shown in Figure 8(a). When the nappe flow reaches a drowned condition, the pressure seems almost hydrostatic because the voids behind the nappe are filled with water, as shown in Figure 8(c). This effect was difficult to observe during the experimental works. However, the drowned simulation of the weir has a greater size and a spatially minor low-pressure region. If the nappe-flow condition is changed by temporary aeration, the low-pressure zone becomes larger, but its size is decreased. In the current study, drowned nappe produces a similar situation to the behaviour of the ogee weir. In this situation, the low pressure on the downstream face of the labyrinth weir caused increasing the discharge.

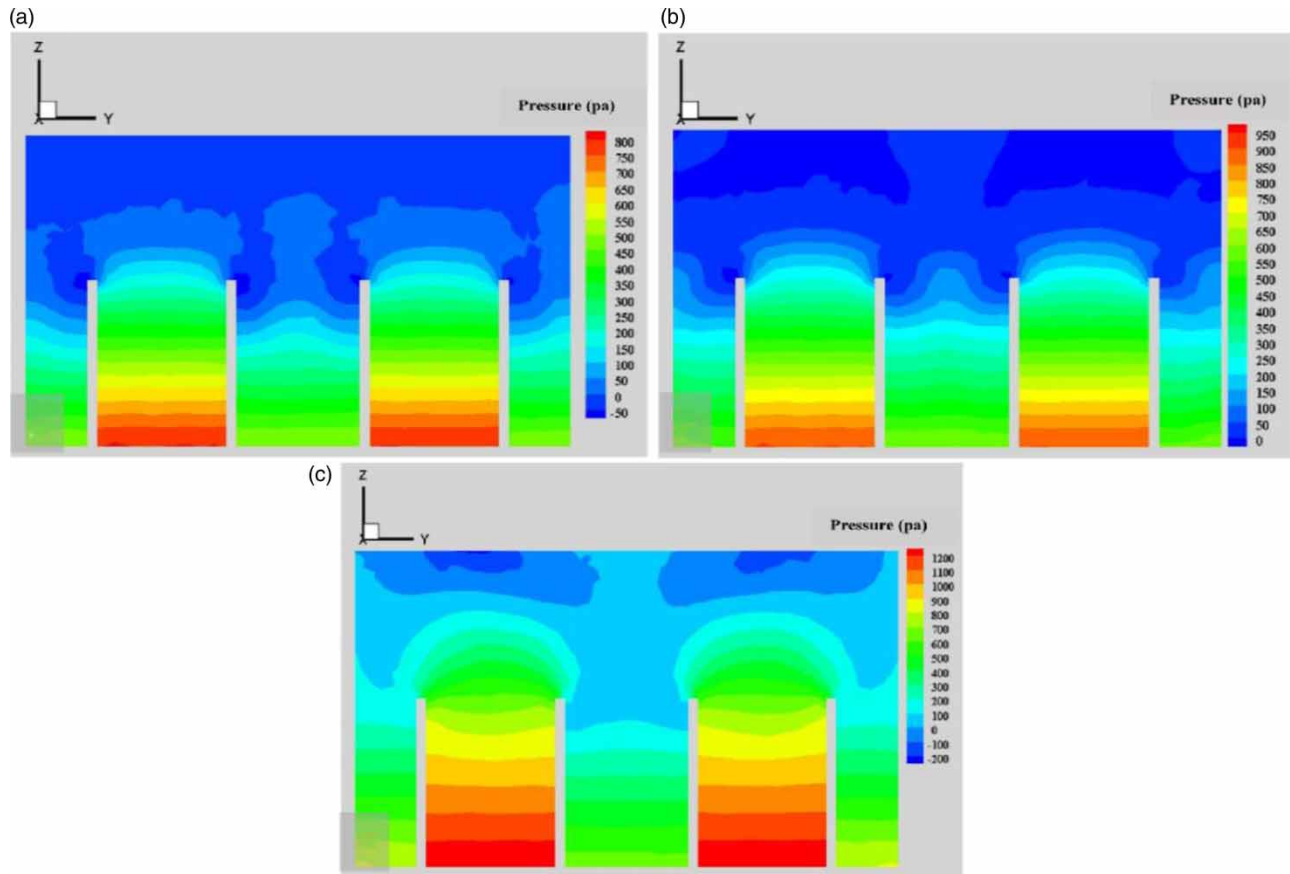


**Figure 8** | Pressure distribution behind nappe flow under flow conditions (a) aerated, (b) partially aerated and (c) drowned. For  $\alpha = 10^\circ$  and  $Q = 0.02 \text{ m}^3/\text{s}$ ,  $0.04 \text{ m}^3/\text{s}$  and  $0.06 \text{ m}^3/\text{s}$ , respectively.

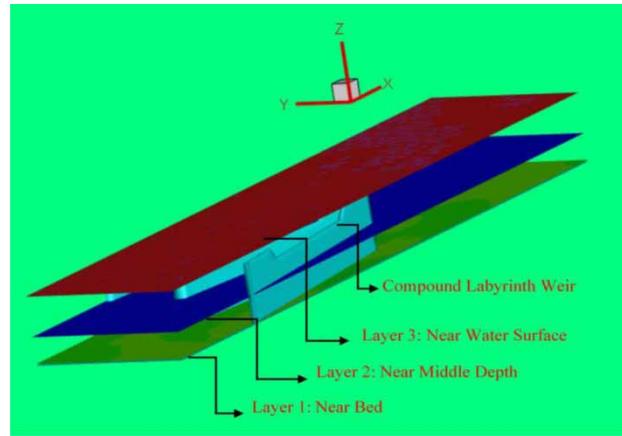
Despite most of the region beneath the nappe being filled with water, in the case of steady-state, there was a small size remaining of the voids that were distributed adjacent to the compound labyrinth weir apexes. In the physical model at the highest heads, coercive air voids were occupied with water and the air was passed downstream. Also, it was observed at the discharge of  $Q > 0.06 \text{ m}^3/\text{s}$  that the strong low-pressure zone reduced slightly because of the drowned nappe condition. In addition, it moved to the larger pressure zones as the discharge continued to increase.

### Simulation of flow streamlines and water surface profile

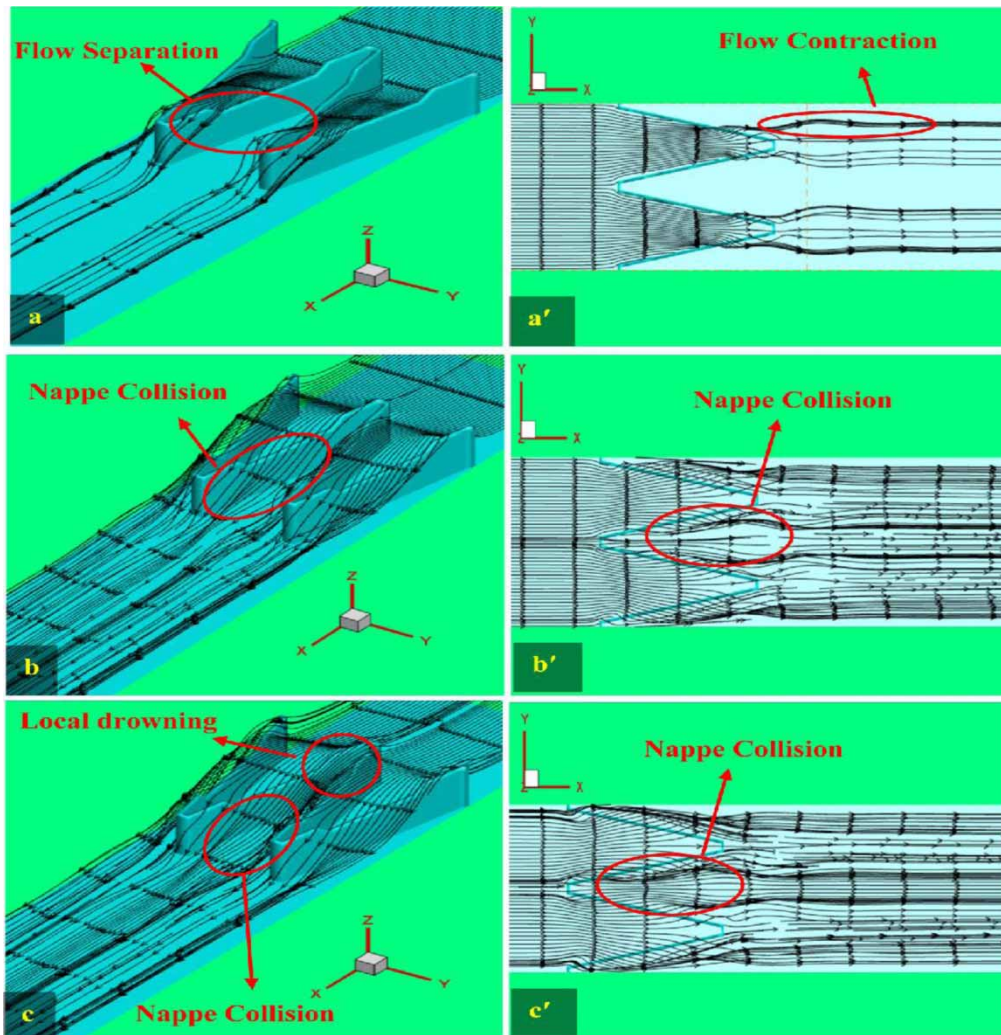
In this section, the flow streamlines, and water surface profile were simulated. The purpose was to find further analysis for the hydraulics performance of the compound labyrinth weir that cannot be detected in an experimental test. Also, it was a sufficient method to determine the reasons for variances in the distribution of the flow pattern along the compound labyrinth weir. In the present study, the horizontal pattern used horizontal slices in three layers of compound labyrinth weir, as shown in Figure 9.

Figure 10 showed flow streamlines and a top view of the water surface shape over a compound labyrinth weir for three layers (e.g. near bed, middle depth, and near-water surface). A sidewall angle ( $\alpha$ ) of  $10^\circ$  was used, and the discharge ( $Q$ ) was  $0.06 \text{ m}^3/\text{s}$ . In general, the flow was divided into two parts when it passes over the compound labyrinth weir. The upper part was passed over the crest weir, and the lower part was passed over the notches.

The pressure is produced from the existence of the perpendicular inlet crest wall of the compound labyrinth weir. The undesirable pressure gradient causes the separation of adjacent streamlines from the bed of the weir. Also, flow streamlines were contracted in the outlet weir, as shown in Figure 10(a, a'). The split streamlines are related to the confusing flow from the upstream wall face and a swirling pattern along the weir. The flow near-bed was complex, and it hit the inlet crest of the vertical wall of the weir. The discharges were mainly passed from the downstream corner of the notches of the compound



**Figure 9** | Location of the slices in the near bed, middle depth and near water surface of the compound labyrinth weir.



**Figure 10** | 3D Flow streamlines and top view of water surface shape over a compound labyrinth weir for three layers in (a, a'), near bed (b, b') middle depth and (c, c') near water surface for  $\alpha = 10^\circ$  and  $Q = 0.06 \text{ m}^3/\text{s}$ .

labyrinth weir, and contractions of the streamlines can be observed in the mid-depth layer of the weir. The flow complexity between sidewalls of the compound labyrinth weir can cause significant energy loss, thus reducing the  $C_{dc}$ .

In case the flow in the mid-depth of the compound labyrinth weir, most streamlines are concentrated over notches of the weir. Also, it was observed that the water surface was raised strongly over the end of the weir. This is attributed to the discharge capacity of the inlet crest being limited, as presented in Figure 10(b, b'). This phenomenon increases the weir obstruction. Also, the nappe collision begins to appear. In the case of flow in the near-water surface layer, streamlines show the clear occurrence of nappes collision and local submergence over the compound labyrinth weir, as shown in Figure 10(c, c'). At the near-water surface layer, the hydraulics behaviour of the compound labyrinth weir is similar to the oblique and linear weirs when the flow is high. This is attributed to the distribution of the streamlines at the water surface layer being more uniform over a compound labyrinth weir when the flow is high value. Furthermore, this phenomenon is attributed to the jet falling angle over the sidewall crest of the compound labyrinth weirs.

### Velocity distribution simulation

Velocity distribution over compound labyrinth weirs considers a significant factor in designs like this type of hydraulic structure because it provides insight into the critical regions that should be considered when designing compound labyrinth weirs. Figure 11 showed contour plots that represent the distribution of velocity and velocity vectors along compound labyrinth weir. Sidewalls ( $\alpha$ ) of  $10^\circ$  have been used, and three discharges ( $Q$ ) of  $0.02 \text{ m}^3/\text{s}$ ,  $0.04 \text{ m}^3/\text{s}$  and  $0.06 \text{ m}^3/\text{s}$  have been applied.

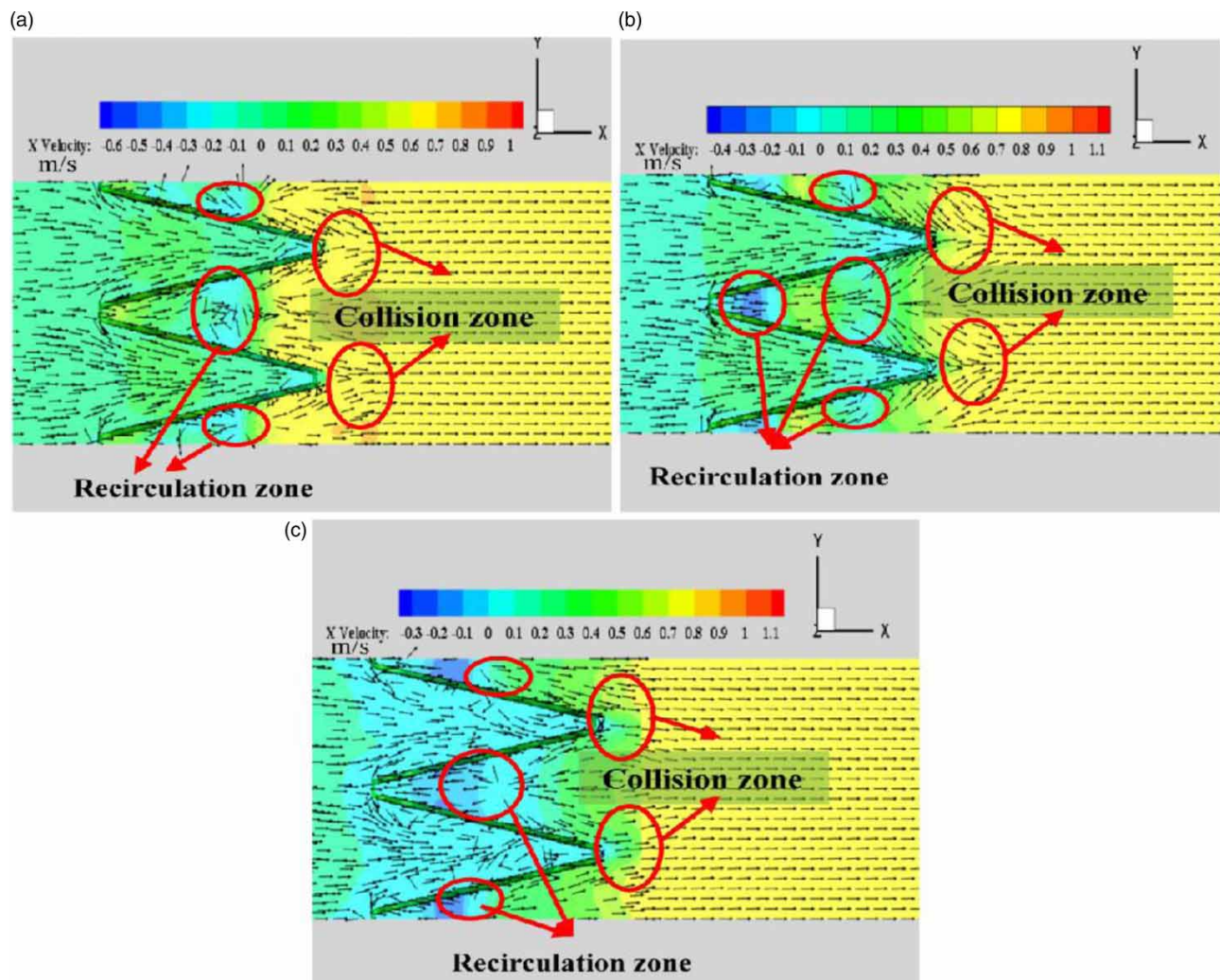


**Figure 11** | Distribution of velocity along compound labyrinth weir for  $\alpha = 10^\circ$  and (a)  $Q = 0.02 \text{ m}^3/\text{s}$ , (b)  $Q = 0.04 \text{ m}^3/\text{s}$  and (c)  $Q = 0.06 \text{ m}^3/\text{s}$ .

Figure 11 showed that the distribution of velocity was uniform and had a high-velocity magnitude downstream of the weir, while the velocity distribution was nonuniform upstream of the weir. Also, Figure 11 indicated clear separation velocity vectors upstream of the weir, especially at upstream apex zones and notches. This result is attributed to the obstruction of the weir structure. Negative velocities were observed near the outlet flow of the notches and outlet flow of upstream apexes, these velocities indicate the recirculation phenomena in these zones.

The distribution of velocity along the weir also shows that the existing recirculation phenomena are represented in blue colour and collision velocity vectors, especially at the outlet flow of the notch's zones, as illustrated in Figure 11(a) and 11(b) for low discharge ( $Q = 0.02 \text{ m}^3/\text{s}$ ) and medium discharge ( $Q = 0.04 \text{ m}^3/\text{s}$ ). In addition, at high discharge ( $Q = 0.06 \text{ m}^3/\text{s}$ ), the recirculation phenomena were extended to the outlet flow of upstream apexes, as shown in Figure 11(c). The effectiveness of the recirculation zones decreases with increasing cell width of the weir toward the downstream which, caused streamline concentration and thus increased flow velocities. Figure 11 also demonstrates collision zones at downstream apexes, as represented by velocity vectors. Figure 11 showed that the flow velocity delivering through the notches was bigger than the flow velocity over the compound labyrinth weir crest. However, the high velocity in the notch zones facilitates great discharges to pass over the compound labyrinth weir.

## CONCLUSION

To improve the understanding of the hydrodynamics flow of the trapezoidal compound labyrinth weirs, the CFD model was used to simulate the flow characteristics for different flow conditions of the compound labyrinth weir. The findings of the current study showed that there is a good agreement between the experimental and CFD results. The CFD results demonstrated that the nappe flow conditions such as aerated, partially aerated, and drowned were similar to observations of the physical model. In the middle of notches of the labyrinth weir, the energy dissipation occurred in local regions behind nappe flow. The simulation confirmed existing the air cavities and bubbles in separated places behind the nappe flow. Also, in the middle of notches, the shape and size of vortices have changed with increased discharge. The low-pressure zones developed larger with lower magnitude. The low-pressure zones were slightly decreased when the discharge was bigger than  $0.06 \text{ m}^3/\text{s}$ . Furthermore, the CFD results showed that streamlines over the compound labyrinth weir were divided into two parts. Part of the streamlines passed over the labyrinth weir crest and the other part passed over the notches. The streamline contractions were observed in the mid-depth layer of the weir. Most streamlines were concentrated over the notches of the weir. The nappe collision has occurred near the water surface layer of the compound labyrinth weir.

The results demonstrated that the hydraulic behaviour of the compound labyrinth weir was similar to the oblique and linear weirs in high discharges. Moreover, the distribution of velocity was uniform and had a high-velocity magnitude downstream of the compound labyrinth weir, while the velocity distribution was nonuniform upstream of the weir. The velocity vectors upstream of the weir were separated, especially at upstream apex zones and notches. In addition to negative velocities have been observed near the outlet flow of the notches and outlet flow of upstream apexes. The recirculation zones effectively decreased with increasing cell width of the weir toward the downstream, which caused streamline concentration and thus increasing flow velocity over the weir. Also, the distribution of velocity along the weir indicated the existing recirculation phenomena especially at an outlet flow of the notch zones for low discharge ( $Q = 0.02 \text{ m}^3/\text{s}$ ) and medium discharge ( $Q = 0.04 \text{ m}^3/\text{s}$ ). In contrast, at high discharge ( $Q = 0.06 \text{ m}^3/\text{s}$ ), recirculation phenomena were extended to the outlet flow of upstream apexes. Also, the flow velocity passing through the notches was bigger than the flow velocity over the entire compound labyrinth weir. The high velocity in the notch zones was greater discharges than through the entire compound labyrinth weir.

## ACKNOWLEDGEMENTS

The authors would like to express their sincere thanks and gratitude to the Iraqi government for providing financial support for the study. The authors also express their sincere thanks to the school of engineering/Deakin University for using the test facility. Also, they are thankful for the laboratory staff at the School of Engineering (Deakin University).

## DATA AVAILABILITY STATEMENT

All relevant data are included in the paper or its Supplementary Information.

## REFERENCES

- Ackers, J., Bennet, F. & Zamesky, G. 2011 Upgrading Lake Holiday spillway using a labyrinth weir. In *Proc. 31st Annual USSD Conference*, San Diego, California, pp. 1683–1696.
- Bhuiyan, F. A. B. M. & Hey, R. 2007 [Computation of three-dimensional flow field created by weir-type structures](#). *Engineering Applications of Computational Fluid Mechanics* **1** (4), 350–360.
- Bilhan, O., Aydin, M. C., Emiroglu, M. E. & Miller, C. J. 2018 [Experimental and CFD analysis of circular labyrinth weirs](#). *Journal of Irrigation and Drainage Engineering* **144** (6), 04018007.
- Carrillo, J. M., Matos, J. & Lopes, R. 2019 Numerical modeling of free and submerged labyrinth weir flow for a large sidewall angle. *Environmental Fluid Mechanics* **20** (2), 1–18.
- Carrillo, J. M., Matos, J. & Lopes, R. 2020 [Numerical modeling of free and submerged labyrinth weir flow for a large sidewall angle](#). *Environmental Fluid Mechanics* **20** (2), 357–374.
- Choufu, L., Abbasi, S., Poursahbaz, H., Taghvaei, P. & Tfwala, S. 2019 Investigation of flow, erosion, and sedimentation pattern around varied groynes under different hydraulic and geometric conditions: a numerical study. *Water* **11** (2), 235.
- Crookston, B. M. 2010 *Labyrinth Weirs. Doctor of Philosophy (Phd) Dissertation*, Utah State University, Logan, UT.
- Dabbling, M. R. 2014 *Nonlinear Weir Hydraulics*. M.Sc. Thesis, Utah State University, USA.
- Daneshfaraz, R., Ghahramanzadeh, A., Ghaderi, A., Joudi, A. R. & Abraham, J. 2016 [Investigation of the effect of edge shape on characteristics of flow under vertical gates](#). *Journal-American Water Works Association* **108** (8), E425–E432.
- Daneshfaraz, R., Minaei, O., Abraham, J., Dadashi, S. & Ghaderi, A. 2019 [3-D numerical simulation of water flow over a broad-crested weir with openings](#). *ISH Journal of Hydraulic Engineering* **27** (s1), 1–9.
- Ghaderi, A., Daneshfaraz, R., Abbasi, S. & Abraham, J. 2020 [Numerical analysis of the hydraulic characteristics of modified labyrinth weirs](#). *International Journal of Energy and Water Resources* **4** (4), 425–436.
- Ghare, A. D., Mhaisalkar, V. A. & Porey, P. D. 2008 An approach to optimal design of trapezoidal labyrinth weirs. *World Applied Sciences Journal* **3** (6), 934–938.
- Hirt, C. W. & Nichols, B. D. 1981 Volume of fluid (VOF) method for the dynamics of free boundaries. *Journal of Computational Physics* **39** (1), 201–225.
- Holmquist-Johnson, C. L. 2011 *Numerical Analysis of River Spanning Rock U-Weirs: Evaluating Effects of Structure Geometry on Local Hydraulics. Doctoral Dissertation*, Colorado State University, Fort Collins, CO.
- Hu, H., Qian, Z., Yang, W., Hou, D. & Du, L. 2018 [Numerical study of characteristics and discharge capacity of piano key weirs](#). *Flow Measurement and Instrumentation* **62**, 27–32.
- Idrees, A. K., Al-Ameri, R. & Das, S. 2016 Determination of discharge coefficient for flow over one cycle compound trapezoidal plan form labyrinth weir. *International Journal of Civil Engineering and Technology* **7** (4), 314–328.
- Institute for Water and Environmental Engineering 2012 Investigation of unsteady flow conditions at dam bottom outlet works due to air entrainment during gate closure. In: *Volume II: Computational Modelling*. Water Research Commission, Gezina.
- Kheirkhah Gildeh, H. 2013 *Numerical Modeling of Thermal/Saline Discharges in Coastal Waters. Doctoral Dissertation*, Université d'Ottawa/University of Ottawa, Ottawa, ON.
- Lopes, R., Matos, J. & Melo, J. 2008 Characteristic depths and energy dissipation downstream of a labyrinth weir. In *proc. of the int. Junior Researcher and Engineer Workshop on Hydraulic Structures (IJREWS '08)*, 2008, Pisa, Italy, pp. 51–58.
- Paxson, G., Crookston, B., Savage, B., Tullis, B. P. & Lux, F. 2008 The hydraulic design toolbox: Theory and modeling for the Lake Townsend Spillway replacement project. *Association of State Dam Safety Officials (ASDSO)*.
- Poursahbaz, H., Abbasi, S., Pandey, M., Pu, J. H., Taghvaei, P. & Tofangdar, N. 2020 [Morphology and hydrodynamics numerical simulation around groynes](#). *ISH Journal of Hydraulic Engineering*, 1–9.
- Salazar, F. & Crookston, B. M. 2019 [A performance comparison of machine learning algorithms for arced labyrinth spillways](#). *Water* **11** (3), 544.
- Sangsefidi, Y., Mehraein, M. & Ghodsian, M. 2015 Numerical simulation of flow over labyrinth spillways. *Scientia Iranica* **22** (5), 1779–1787.
- Sangsefidi, Y., MacVicar, B., Ghodsian, M., Mehraein, M., Torabi, M. & Savage, B. M. 2019 [Evaluation of flow characteristics in labyrinth weirs using response surface methodology](#). *Flow Measurement and Instrumentation* **69**, 101617.
- Savage, B., Frizell, K. & Crowder, J. 2004 Brains versus brawn: the changing world of hydraulic model studies. In *Proceedings of the (2004) Annual Conference*, Phoenix, USA. Association of State Dam Safety Officials (ASDSO).
- Savage, B. M., Crookston, B. M. & Paxson, G. S. 2016 [Physical and numerical modeling of large headwater ratios for a 15 labyrinth spillway](#). *Journal of Hydraulic Engineering* **142** (11), 04016046.
- Seo, I. W., Do Kim, Y., Park, Y. S. & Song, C. G. 2016 [Spillway discharges by modification of weir shapes and overflow surroundings](#). *Environmental Earth Sciences* **75** (6), 1–13.
- Shafiei, S., Najarchi, M. & Shabanlou, S. 2020 [A novel approach using CFD and neuro-fuzzy-firefly algorithm in predicting labyrinth weir discharge coefficient](#). *Journal of the Brazilian Society of Mechanical Sciences and Engineering* **42** (1), 1–19.
- Shaghaghian, M. & Sharifi, M. 2015 [Numerical modeling of sharp-crested triangular plan form weirs using FLUENT](#). *Indian Journal of Science and Technology* **8** (34), 1–7.

- Shaheed, R., Mohammadian, A. & Gildeh, H. K. 2019 A comparison of standard  $k-\epsilon$  and realizable  $k-\epsilon$  turbulence models in curved and confluent channels. *Environmental Fluid Mechanics* **19** (2), 543–568.
- Smith, G. N. 1986 *Probability and Statistics in Civil Engineering*. Collins professional and technical books, New York, NY, p. 244.
- Torres, C., Borman, D., Sleigh, A. & Neeve, D. 2018 Determination of Scale Effects for A Scaled Physical Model of A Labyrinth Weir Using CFD.
- Tullis, J. P., Amanian, N. & Waldron, D. 1995 Design of labyrinth spillways. *Journal of Hydraulic Engineering* **121** (3), 247–255.
- Versteeg, H. & Malalasekera, W. 1995 *An Introduction to Computational Fluid Dynamics*. Longman Scientific and Technical, Harlow.
- Yildiz, A., Marti, A. I. & Gogus, M. 2021 Determination of hydraulic characteristics of flow over a triangular sectioned weir by using experimental and numerical modeling. *Journal of Computational Applied Mechanics* **52** (2), 215–232.

First received 17 September 2021; accepted in revised form 22 November 2021. Available online 7 December 2021